# Growth of Black, Violet, and FCC Arsenic Phosphorus Thin Films

Nezhueyotl Izquierdo<sup>1</sup>, Jason C. Myers<sup>2</sup>, Prafful Golani<sup>3</sup>, Adonica De Los Santos<sup>4</sup>, Nicholas C. A. Seaton<sup>2</sup>, Steven J. Koester<sup>3</sup>, and Stephen A. Campbell\*<sup>3</sup>

E-mail: \*scampbell@umn.edu

# Abstract

Black arsenic phosphorus single crystals are grown using a short-way transport technique that results in crystals up to  $12 \times 110$  microns and range from 200 nm to 2 microns thick. The reaction conditions require tin, tin(IV) iodide, grey arsenic, and red phosphorus placed in an evacuated quartz ampule and ramped up to a maximum temperature of 630 °C. The crystal structure and elemental composition were characterized using Raman spectroscopy, x-ray diffraction, and x-ray photoelectron spectroscopy, cross-sectional transmission microscopy and electron backscatter diffraction. The data provides valuable insight into the growth mechanism. A previously developed b-P thin film growth technique can be adapted to b-AsP film growth with slight changes to the procedure. Devices fabricated from exfoliated bulk-b-AsP grown in the same conditions as the thin film growth process are characterized, showing an on-off current ratio of  $10^2$ , a threshold voltage of -60 V, and a peak field-effect hole mobility of  $23 \text{ cm}^2/\text{V} \cdot \text{s}$  at  $V_d$ =-0.9 and  $V_g$ =-60 V.

Keywords: two-dimensional, black arsenic phosphorus, black phosphorus, thin film, crystal growth,

# 1. Introduction

Two dimensional (2D) materials have seen a surge of interest since the initial influx of graphene literature published in the early 2000's. This rise in 2D material interest may be attributed to the intriguing qualities of 2D materials for electronic and opto-electronic devices, such as the potential for van der Waals heterostructures with pristine interfaces, layer modulated bandgaps, quantum confined nanostructures, and a plethora of other exciting materials properties. The ever-expanding list of 2D materials include insulators, semiconductors, semimetals, and metals. The materials are unique in structure and possess properties that expand the engineer's material toolbox.

The creation of high quality, large area, uniform thin film 2D material synthesis is a crucial materials engineering

challenge for 2D materials to become a viable option for device commercialization. Differing 2D synthesis methods have comparative advantages and disadvantages, such as synthesis time-constraints, product purity, and potential for large-scale commercialization. In this paper, we demonstrate the deposition of thin film black arsenic phosphorus (b-AsP) single crystals on an oxidized silicon wafer. The results provide valuable experimental insight into how the short-way transport growth mechanism proceeds.

Alloying black phosphorus (b-P) with As to form black arsenic phosphorus with varying As composition allows one to fine-tune the bandgap from 0.3 (b-P) to 0.15 eV (b-As) for bulk crystals.<sup>3</sup> As with other 2D materials, the bandgap also depends on the number of layers, up to a critical thickness. Thereafter, the material exhibits bulk bandgap properties that are independent of the number of layers.<sup>4</sup> b-P is well known to be susceptible to surface oxidation due to interaction with

xxxx-xxxx/xx/xxxxxx 1 © xxxx IOP Publishing Ltd

<sup>&</sup>lt;sup>1</sup>Department of Chemical Engineering and Materials Science, University of Minnesota, Minneapolis, United States

<sup>&</sup>lt;sup>2</sup>Characterization Facility, University of Minnesota, Minneapolis, United States

<sup>&</sup>lt;sup>3</sup>Department of Electrical and Computer Engineering, University of Minnesota, Minneapolis, United States

<sup>&</sup>lt;sup>4</sup>Department of Mechanical Engineering, University of Texas Rio Grande Valley, Edinburg, United States

H<sub>2</sub>O and UV light.<sup>5-9</sup> In addition to changing the bandgap, the incorporation of As into the b-P lattice also significantly improves the stability.<sup>3</sup> Thus far, literature reports of b-AsP thin film devices focus on the material's electronic and optical properties to fabricate thin film transistors and mid-infrared photodetectors, however, recent publications have extended b-AsP applications for battery and photovoltaic devices.<sup>3,10</sup>

b-P is an orthorhombic crystal system with lattice dimensions a = 3.3133 Å, b=10.473 Å, c = 4.373 Å, and  $\alpha = \beta$ =  $\gamma = 90^{\circ}$ . Introducing arsenic into the b-P lattice increases the lattice parameters. 12 According to computational literature on b-AsP, a thermodynamic shift in crystal structure stability from orthorhombic to trigonal occurs at an As concentration of x=0.83 for b-As<sub>x</sub>P<sub>1-x</sub>.  $^{12}$  The b-AsP crystal lattice parameters are predicted to follow a linear increase up to the phase transition point, supported by Vegard's Law.12 Up until recently, pure bulk b-As had yet to be fabricated in a laboratory, however naturally occurring black As, commonly referred to by Arsenolamprite, had been reported.<sup>13</sup> This naturally-occurring bulk black arsenic can be sourced from Chilean mines.<sup>13</sup> However, two recent publications have reported the ability to purchase b-As crystal from commercial vendors.14,15

Forming bulk b-AsP crystals with varying compositions has been shown to be a relatively simple, albeit slow and inefficient process. The direct growth of bulk black arsenic phosphorus alloy crystals (b-As<sub>x</sub>P<sub>1-x</sub>) under very high pressure was first reported by Shirotani et. al for x=0.05 and x=0.1. Black As (87% As) alloyed with mercury (Hg) has also been synthesized by reacting grey Arsenic (g-As) and Hg at 100-200 °C for 7 days. 17 A recent report demonstrated synthesis of bulk b-AsP alloy using a short-way transport technique with the precursors tin (Sn), tin(IV) iodide (SnI<sub>4</sub>), red phosphorus (r-P), and g-As at a more moderate pressure compared to Shirotani.<sup>3,16</sup> In this process, the vapor pressure of the constituent species is a first-order parameter. The pressure can be estimated using the Antoine equation with constants provided by NIST.18 At the bulk crystal growth reaction maximum soak temperature of 630 °C, g-As and r-P are both found in their tetramer vapor form, As<sub>4</sub> and P<sub>4</sub>, respectively.<sup>19</sup> According to equilibrium vapor pressure calculations, As contributes < 2% of the combined g-As and r-P total pressure at 630 °C.

Wafer scale thin films of b-AsP have only been demonstrated by molecular beam deposition, providing synthesis of b-As.78P.22 on an InP substrate. The resultant films had very small (~5 nm) grains, <sup>20</sup> which would likely lead to poor electrical behavior. In a previous paper we demonstrated that the short-way transport growth process for bulk b-P could be modified for thin film growth. <sup>21</sup> There we demonstrated

that the Sn concentration did not impact the crystal phase as long as there was a sufficient amount in the ampule. In contrast, the SnI4 concentration is the primary parameter that affects thin film growth, especially the crystal phase. SnI4 is also known to promote Sn transport since Sn is a low equilibrium vapor pressure material.<sup>22</sup> We had two main findings regarding the b-P growth mechanism. First, there is a Sn in-situ passivation layer (2-5 nm) surrounding the bulk and thin film crystals, as determined by cross-sectionan transmission eletron microscopy (CS-TEM) and x-ray photoelectron spectroscopy (XPS).<sup>21</sup> Second, Sn-I rich inclusion crystals are found to be scattered throughout the crystal at different crystal layer heights. These Sn-I rich inclusion particles form epitaxially with the b-P lattice and could function as nucleation centers.

Here we report on the growth of b-AsP thin films on an oxidized silicon wafer. CS-TEM and Raman spectroscopy show highly crystalline materials. However, high resolution TEM indicates the presence of an *in situ* Sn passivation layer, As precipitates in the film, and an underlying amorphour layer. We also present exfoliated b-AsP thin film transistor device data.

## 2. Methods

### 2.1. Crystal Growth

b-AsP growth directly onto a silicon or silicon oxide wafer is fabricated using the following reactants: g-As (Sigma Aldrich, 99.999%), r-P (Sigma Aldrich, 99.99%), SnI<sub>4</sub> (Alfa Aesar, 99.998%), and Sn foil (Sigma-Aldrich, 99.8%, 0.127 μm thickness). The r-P and SnI<sub>4</sub> reactant mass was varied in order to study the effect of each reactant on the growth process. Each experiment is shown in Figure 1. A quartz glass tube (10.5 mm ID, 15.8 mm OD, and a length of 10 cm) with one rounded end is cleaned using a standard solvent wash and placed into a glass oven at 120 °C for 5 minutes. All reactant material is placed into the quartz ampule inside of a nitrogen glove box. Wafer pieces are cleaned by solvent sonication wash and placed inside of the ampule with the reactant material. The ampule and its contents are evacuated and sealed under vacuum (10<sup>-5</sup> Pa) with an oxyacetylene torch. The temperature profile is controlled in a Thermo Scientific Lindberg Blue M three-zone tube furnace with programmable PID controllers. The ampule is placed across the diameter of the furnace tube to promote a uniform temperature in the ampule. The thin film b-AsP reaction proceeds for a total of 26.5 hours. The initial ramp-up process starts at room temperature and increases to 630 °C (maximum soak temperature) at a rate of 152.5 °C/hr. The maximum soak temperature is held for 8 hours before the temperature is reduced to 250 °C at a rate of 286 °C/hr. The furnace is set to

room temperature and the ampule is allowed to cool over the course of 1 hr.

### 2.2. Characterization

Confocal Raman spectroscopy (Witec Alpha 300R) measurements were performed on b-AsP grown directly onto a silicon or silicon oxide substrate. A 514.5 nm argon laser was used as the excitation source, and the Ag1, B2g, and Ag2 BP phonon modes are found at 360.5, 436.5, and 464 cm<sup>-1</sup>. A Keyence VHX-5000E microscope was used for optical microscopy imaging using depth composition imaging. AFM (Bruker Nanoscope V Multimode 8 with QNM) line profile depth analysis of b-AsP flakes is achieved using Gwyddion software. A JEOL 6500 field-emission scanning electron microscope (SEM) equipped with an EBSD detector is used to analyze the crystal orientation and asses epitaxial growth relationship of b-AsP and the wafer. A b-AsP CIF file was not available at the time of EBSD analysis. However, due to the similarities in crystal structure (i.e. orthorhombic, within 5-10% of lattice parameters), the b-P CIF file was able to index the b-AsP properly. This was validated with the CS-TEM experiment. The following CIF file parameters were used to index b-AsP: lattice parameters, a = 3.3133, b = 10.473, c =4.373,  $\alpha = \beta = \gamma = 90^{\circ}$ , and the space group Cmca. EBSD maps produced by Oxford Instruments Channel 5 software operated with 20 kV accelerating voltage and ~20 nA for the e-beam.

The following section details the device fabrication process. Heavily doped silicon substrates were placed in a Tylan furnace with a flow of dry oxygen for approximately 45 minutes at 1000 °C to form a 50 nm thermal oxide on the surface. Device work used this thermal oxide as the gate insulator for all b-AsP transistors. Mechanical exfoliation of b-AsP was achieved using PDMS stamps formed on a glass slide. Bulk b-AsP crystals formed in the thin film b-AsP ampule are used for device formation. An electron beam evaporator (SEC-600) was used to deposit a Ti (10 nm)/Au (100 nm) metal contact stack.

## 2. Results

As with our previous study, the reaction parameters were first investigated to determine the optimal SnI<sub>4</sub>/P mass ratio for growing thin film b-AsP. The quartz ampule had a volume of 16.6 cm<sup>3</sup>. The amount of As (400 mg) and Sn (18.5 mg) were held constant throughout the growth parameter study. As/P reactant molar ratios were varied by changing the amount of P. The results are shown in Figure 1 and a complete reaction mass conditions table is depicted in S. Figure 1. The plot shows three distinct regions corresponding to 1:1, 1:2, and 1:3 As/P molar ratios. There are three different AsP alloyed structures corresponding to violet (red diamond, v-AsP), face centered cubic (green triangle, FCC or c-AsP), and black

(black square). An image of the reaction ampule after a completed reaction is shown in S. Figure 1a, as well as three optical microscopy images of v-AsP, c-AsP, and b-AsP (S. Figure b-d) thin films. The growth condition indicated by a blue circle forms mixed c-AsP and black AsP thin films. v-AsP is found at only one composition in our reaction parameter study, SnI<sub>4</sub>/P=0.05 and As/P=1/3. We believe this to be the first report of v-AsP growth. A third structure, c-AsP, is found for SnI<sub>4</sub>/P=0.08 and 0.11 and As/P=0.33. Increasing the As/P molar ratio to 1:2 shifts the preferred alloy structure to a combination of both the mixed and orthorhombic structures. Upon further increasing the SnI<sub>4</sub> concentration only the b-AsP alloy structure forms. b-AsP forms in the 1:1 As/P molar ratio regime at all concentrations of SnI<sub>4</sub>. Therefore, a 1:1 As/P molar ratio is preferred to grow b-AsP crystals.

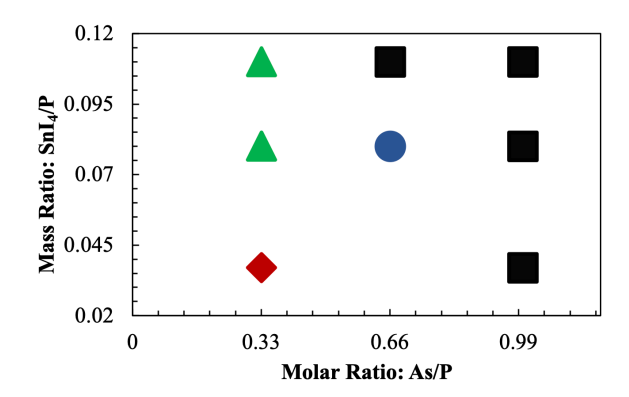


**Figure 1:** Mass Ratio: SnI<sub>4</sub>/P vs. Molar Ratio: As/P reaction parameter plot. Different AsP phases are marked for v-AsP (violet diamond), c-AsP (green triangle), black AsP (black square) and mixed c-AsP/b-AsP (blue circle) growth conditions.

Large, ~0.5 cm long, bulk b-AsP crystals form along the bottom of the ampule when growing with the 1:1 As:P conditions. It should be noted, traces of yellow As and white P are also distributed along the ampule bottom. Precautions should be taken to avoid inhaling any fumes that arise from opening the ampules. All ampules in this experiment were opened in a glove box, transferred to a fume hood and allowed to vent before analysis was attempted.

The total arsenic concentration in the reaction was found to have limited effect on the As concentration of the resulting b-AsP crystals grown directly on the wafer. b-AsP crystals grown on the surface of the wafer have a wide variance in As composition. Figure 2 shows representative Raman spectra for low (20%), medium (40%), and high As (70%) compositions. Several experiments were conducted with longer reaction durations (72 hours) in an attempt to better understand the reaction kinetics and the concentration relationship. The experiments were not successful in increasing the maximum arsenic concentration in the flakes, however the As

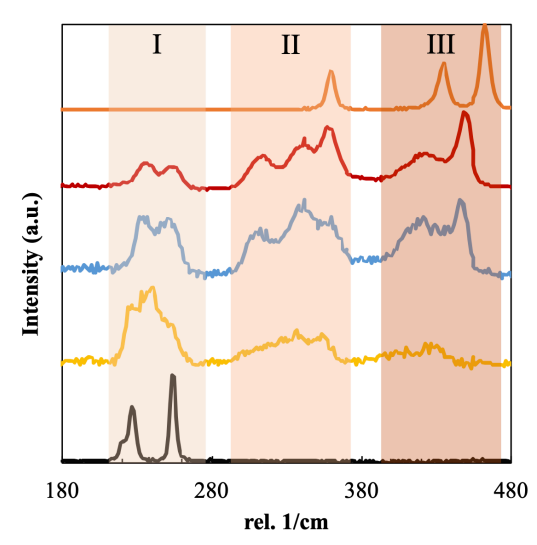


**Figure 2.** Raman spectroscopy of b-P (orange), b-As (black), and b-AsP with varying As concentrations: 20% (red), 40 % (blue), and 70% (yellow).

concentrations in cyrstals grown on the same wafer were more uniform. Optimal growth conditions were found to be identical for thermally grown SiO<sub>2</sub> and bare Si wafers. As expected for 2D material growth, the wafer does not play a critical role in the growth process. Electron backscatter diffraction (EBSD) confirmed that the resultant single crystals grow in random orientations on the surface of the wafer.

The Raman spectra (Figure 2) for b-P and b-AsP were determined experimentally from thin film samples, and the b-As spectra (Arsenolamprite, 532 nm source) was obtained from a mineral database.<sup>23</sup> The three-characteristic b-P Raman peaks Ag<sup>1</sup>, B2g, and Ag<sup>2</sup> BP phonon modes are found at 360.5, 436.5, and 464 cm<sup>-1</sup>, respectively (Figure 2, blue line). b-AsP spectra have three regions labeled I, II, III that correlate with different bonding environments As-As (200-275 cm<sup>-1</sup>), P-As

(375-475 cm<sup>-1</sup>) and P-P (300-380 cm<sup>-1</sup>). The following observations are experimentally verified through our work and agree with published Raman spectroscopy data for b-P, b-AsP, and b-As. 12,24,25 The incorporation of a modest amount of As ( $\sim$ 20%, red) in b-AsP causes the B<sub>2g</sub>, and A<sub>g</sub><sup>2</sup> Raman modes to redshift and merge into a broad peak with a significant reduction in peak FWHM. Further addition of As (~40%, blue) into the b-P lattice results in the formation of a midrange (300-375 cm<sup>-1</sup>) wavenumber peak. Theoretically, this peak reaches its highest relative height for a 50-50 b-AsP alloy. For the highest As composition (~70%, yellow), regions I has the highest relative peak intensity while regions II and III are decreased sequentially, as expected. The pure b-As Raman spectrum was obtained from Golani et. al showing the complete disappearance of region II and III peaks.<sup>26</sup> b-As show a Raman spectrum consisting of peaks at ~220.1 (outof-plane mode  $A_g^1$ ), ~226.3 (in-plane mode  $B_{2g}$ ), and ~253.6 (in-plane mode  $A_g^2$ ) cm<sup>-1</sup>.

Two other distinct AsP alloy crystal structures, c-AsP and v-AsP, have been characterized by Raman spectroscopy. A stacked Raman spectroscopy plot is presented in S. Figure 2 for c-AsP (green), b-AsP (black), v-AsP (blue), and v-P (orange). The characteristic v-P Raman mode wavenumber range of 100-200 cm<sup>-1</sup> is also present in the v-AsP phase.

The c-AsP material is characterized by the x-ray diffraction pattern presented in S. Figure 3. Two potential structure patterns are present on the XRD pattern plot labeled FCC As and SC P. The FCC As pattern is closely related to the pattern observed with minor shifting to the right indicating that the lattice parameters have increased. This observation agrees with the decreased lattice parameter that is expected with increased phosphorus concentration in the c-AsP alloy.

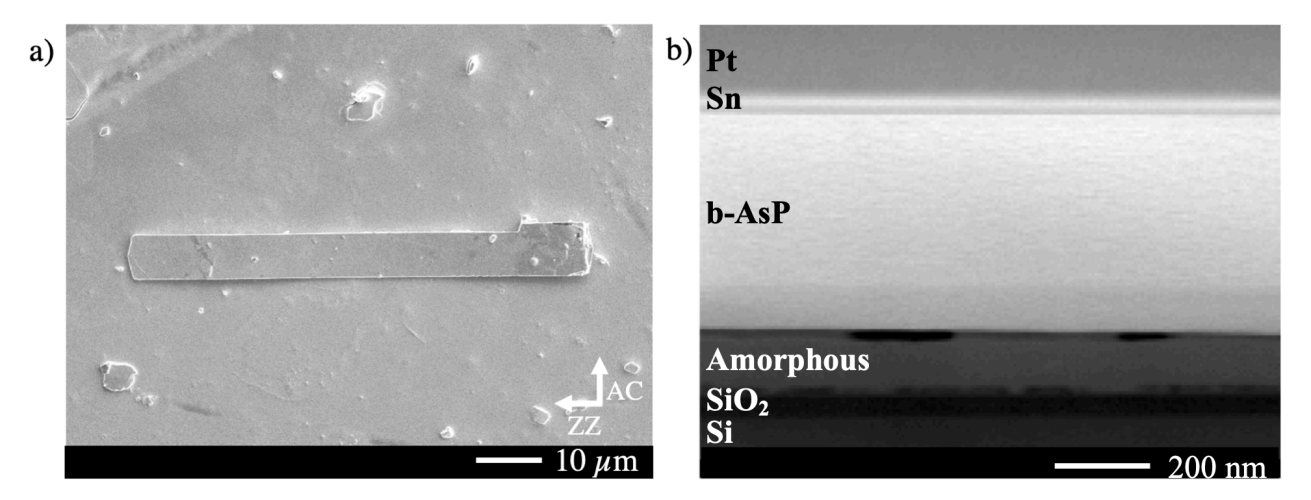


**Figure 3.** a) SEM image of the b-AsP (7 x 70 micron) flake. Armchair and zig-zag orientations are labelled in the bottom right corner. b) CS-TEM: Pt (FIB protective layer), Sn, b-AsP, P/Sn/O, SiO<sub>2</sub>, and Si.

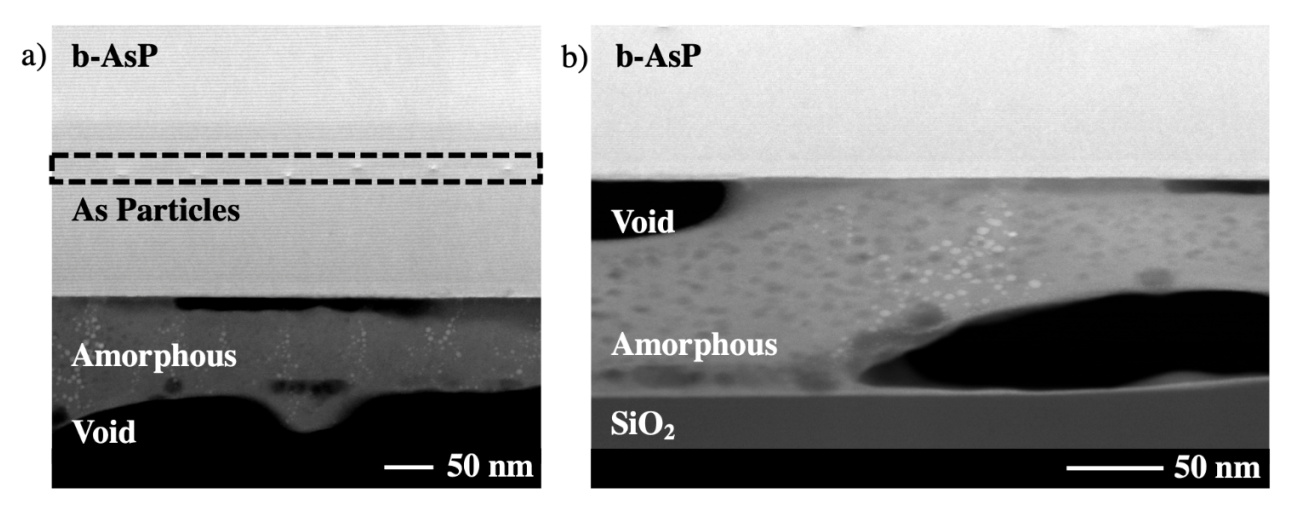


**Figure 4.** CS-TEM analysis of b-AsP. a) black dotted rectangle around As deposits. The following regions are labeled: b-AsP, As particles, amorphous, and void. b) A higher magnification CS-TEM image of b-AsP-amorphous interface and the amorphous-SiO<sub>2</sub> interface.

An SEM image of a thin film b-AsP flake grown on an oxidized Si wafer is depicted in Figure 3a. The crystal is a ~600 nm thick. The CS-TEM image provides no indication of grain boundaries in the b-AsP crystal (Figure 3b). EDS results show that the b-AsP crystal is slightly P rich with 53.5% P and 46.5% As. This atomic ratio does not vary dramatically with vertical position. Arsenic particles (Figure 4a, dotted rectangle) appear in an approximately horizontal line at about 120 nm from the bottom of the crystal. Each As particle is roughly 8 to 10 nm in length and is found along 10 vertical b-AsP layers.

The void layer beneath the b-AsP crystal flake was investigated with electron diffraction spectroscopy (EDS), EDS mapping (S. Figure 4 a-f), and electron energy-loss spectroscopy (EELS) scans to determine the composition and depth of the voids. EDS compositional data indicates that the amorphous layer is homogenous with a composition of Sn<sub>0.07</sub>P<sub>0.20</sub>O<sub>0.71</sub> with trace amounts of Si and As. This suggests that the layer may be a binary SnO2-P2O5 glass. These are generally found to in 50/50 (Sn<sub>0.10</sub>P<sub>0.20</sub>O<sub>0.70</sub>) to 30/70(Sn<sub>0.05</sub>P<sub>0.24</sub>O<sub>0.71</sub>) composition range. They are known for very low glass transition temperatures ranging from 246 to 264 °C.<sup>27</sup> The voids may represent bubbles trapped in the glass as it resolidified. P2O5 has a boiling point of 360 °C, so it is a likely candidate for bubble-forming gas. It is not clear why this material forms in the presence of an As-containing ambient but does not form without the As. A higher resolution image (Figure 4b) shows that the degraded layer height is approximately 200-220 nm with some height variation along the extent of the crystal. An EELS analysis of the void does not show a response, suggesting that the voids extend the entirety of the cross-section. Below the amorphous layer, the SiO<sub>2</sub> is present directly above the Si layer. The SiO<sub>2</sub> layer

thickness is 50 nm, in good agreement with the as-grown thickness. Lastly, the  $SiO_2$  layer does not show any obvious structural degradation. The source of the oxygen may be the ampule walls rather than the thermal oxide.

The b-AsP surface interface is presented in Figure 5. The top-most layer is the carbon coating that is deposited during the FIB process to protect the b-AsP crystal. EDS provides evidence of gallium implantation in the Sn layer. Gallium was used as the ion source for creating the lamella during the cross-section FIB process. FIB damage to the surface of the b-AsP crystal beneath the Sn-rich Ga implanted layer is visible by the loss of crystallinity. The thickness of the Sn-rich Ga implanted layer is 31 nm. The thickness of the Sn-rich layer is mostly

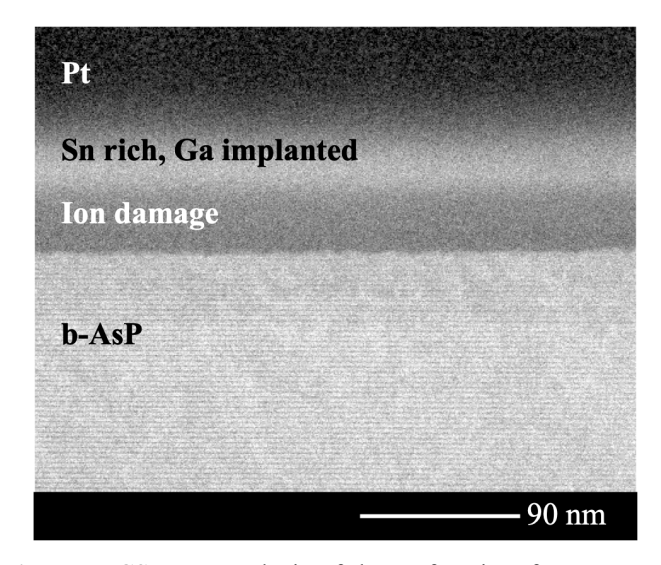


**Figure 5.** CS-TEM analysis of the surface interface. From top to bottom the layers are labelled platinum (Pt), Sn-rich Ga implanted, ion damage, and b-AsP.

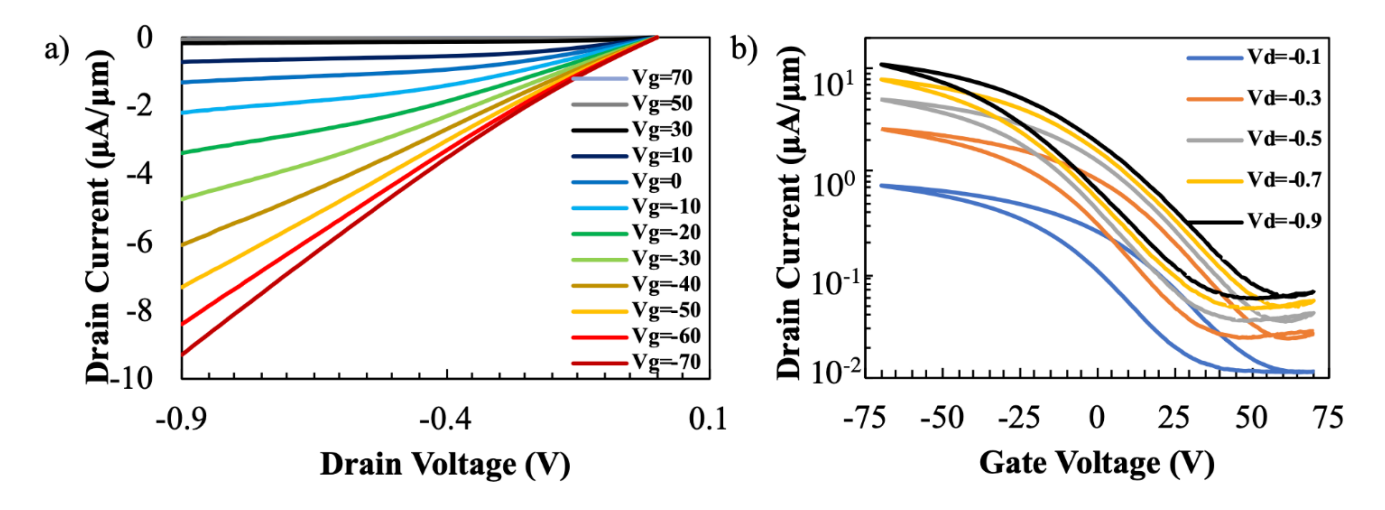


**Figure 6.** Black arsenic phosphorus device characteristics are plotted for drain current as a function of a) drain voltage and b) gate voltage.

uniform across the sample, as can be seen in Figure 3b and Figure 5.

Since black arsenic phosphorus exists as an alloy with varying As concentration, it is difficult to find files with the exact lattice parameters for EBSD software to match the Kikuchi lines. However, the Channel 5 software used here has the ability to match Kikuchi line patterns that have a slight offset from a known structure. In this case, the material was identified with a black phosphorus CIF file of a=3.31 Å, b=10.41 Å, c = 4.373 Å,  $\alpha = \beta = \gamma = 90^{\circ}$ , and space group 64. EBSD results confirm that our b-AsP CS-TEM samples are single crystal. The pole figures presented in S. Figure 3b show that the grown b-AsP (S. Figure 3a) is textured along the caxis (2D stacking direction) normal to the substrate. Interestingly, the preferred crystal growth axis or axis with the longest dimension is along the zigzag, differing from the preferred armchair crystallographic growth axis of black phosphorus grown in our previous study.

Thin film b-AsP devices were fabricated from mechanically exfoliated bulk growth material that was present in the ampule during thin film growth processes. Devices were not fabricated directly on thin film crystals due to the underlying amorphous void layer. To ensure the same growth conditions, however, b-AsP bulk crystals were taken from the bottom of the ampule when b-AsP was grown using optimal thin-film conditions. The b-AsP thin flakes were first mechanically exfoliated from the bulk crystals onto a polydimethylsiloxane (PDMS) stamp via the standard Scotch tape method. Optical microscopy was used to identify the flakes of interest which were then transferred to a 300 nm SiO<sub>2</sub>/Si substrate pre-patterned with identification markers. PDMS was used as a transfer agent as this process minimizes

tape residue on the substrate. The substrate was then washed with acetone and isopropyl alcohol (IPA) to dissolve any existent glue residues. Electron beam lithography on PMMA C4 electron-beam resist was used to pattern openings for the source/drain electrodes. After electron-beam exposure, the samples were developed in a 3:1 mixture of IPA and methyl isobutyl ketone (MIBK) for 90 seconds followed by a short rinse in IPA. A 30 nm/80 nm Ti/Au stack was deposited using electron-beam evaporation followed by liftoff in acetone for 4 hours. The sample was then rinsed in IPA, blown dry with dry nitrogen, and then immediately put inside the cryogenic probe station for electrical characterization. All the measurements were performed using a Keysight B1500A semiconductor parameter analyzer at 25 °C at a pressure of 2 × 10-6 torr.

The device characterized in Figure 6 used a flake with a width of 6.8  $\mu$ m and a source/drain spacing of 1.3  $\mu$ m. The b-As flake thickness is estimated to be  $10 \pm 1.5$  nm. The drain current,  $I_d$ , as a function of drain voltage,  $V_d$ , with the varying gate voltages,  $V_g$ , is presented in Figure 6a. The devices show p-type conduction with an on-state current approaching 10  $\mu$ A/ $\mu$ m at  $V_d$  = -0.9 V and  $V_g$  = -70 V. Figure 6b presents the same device where  $I_d$  is plotted vs.  $V_g$  for five values of  $V_d$ . The on-off current ratio is  $1.66 \times 10^2$  for  $V_d$ =-0.9 with a threshold voltage of +60 V, confirming the p-type conduction. These results are comparable to p-type b-AsP thin film transistors made from material exfoliated from bulk crystals.<sup>8</sup>

# 3. Discussion

Before turning to b-AsP growth, we briefly summarize b-P thin-film growth results for sake of comparison. Ampule experiments conducted with Sn and r-P (excluding SnI<sub>4</sub>) in the source zone under otherwise optimal thin-film growth temperature profile results in no visible growth.<sup>21</sup> The SnI<sub>4</sub>

reactant concentration affects the transport efficiency of Sn and determines the phase selectivity of the thin film phosphorus crystal. Two phosphorus allotropes, violet phosphorus (v-P) and b-P, thin films can be fabricated depending on the SnI<sub>4</sub>/P reactant mass ratio. In-situ passivation of b-P crystals, effective up to at least 70 days air exposure, occur due to the thin film of Sn surrounding the entirety of the crystal. We postulate that a Sn/I/P melt forms and that the free surface of the melt will cool first due to the high thermal mass and excellent thermal conductivity of the silicon wafer. This cooling reduces the solubility of the P, leading to b-P growth. CS-TEM images show epitaxial nanocrystal Sn-I rich particle inclusions that are found throughout the b-P crystals at different heights. These inclusions can function as nucleation centers for subsequent layer growth upon cooling of the melt.

The suggested growth mechanism features aspects of both CVT (Chemical Vapor Transport) and VLS (Vapor Liquid Solid) growth.<sup>28,29</sup> The CVT growth process is a bottom-up approach that uses a metal catalyst. CVT reactions can form single crystals with relative ease. Most CVT reactions require a thermal gradient, forming a vapor concentration gradient within a contained vessel. Volatilization occurs at the higher temperature zone, commonly referred to as the source. The crystallization zone or sink is found at the cold end of the growth vessel. Halogens are commonly used as transport agents for metals with low volatility in CVT reactions.<sup>30–32</sup> A common metal-halogen transport equilibrium equation is expressed as<sup>28</sup>

$$M(s) + \frac{n}{2}I_2(g) \rightleftharpoons MI_n(g)$$

For b-P crystal growth Sn transport can be facilitated by  $I_2$  or  $SnI_4$ .  $^{21,22,33}$   $SnI_4$  is understood to decompose into  $I_2$ .  $^{33}$  The back reaction occurs continuously due to *Le Chatelier's* principle as the  $MI_n$  (g) decomposes to deposit metal in the crystallization zone.  $^{28}$ 

The VLS process can be simplified to three main processes that occur in order for growth to proceed.<sup>34</sup> The first step requires the formation of a liquid alloy droplet on a substrate or preferred growth material. This can either be pre-patterned or occur in-situ during the VLS process. Pre-patterning increases control of the VLS grown material position. The second step requires vapor transport of atoms or molecules to the liquid alloy droplet. The flux of the material can be controlled with the temperature dependent partial pressure of the vapor species. The growth species will adsorb at the vapor-liquid interface and diffuse to the liquid-solid interface. The last step requires that the liquid alloy reach supersaturation and nucleate at the liquid-solid interface to form a solid. The common VLS gold/silicon "whisker" growth process is grown

axially to form high aspect ratios pillars on the substrate.<sup>35</sup> However, VLS growth techniques have been applied to 2D material to grow laterally on the surface of a substrate. For instance, VLS MoS<sub>2</sub> can be grown to form lateral monolayer nano- and microribbons.<sup>36</sup>

Similar to the CVT technique, the b-P and b-AsP growth process both require a transport agent, in this case SnI<sub>4</sub>, to aid in the transport of low equilibrium vapor pressure Sn, however, the crystallization process is more complex considering that the vapors don't condense or crystallize directly from the vapors. In our current growth model, reactants start in the solid phase, then sublime or evaporate, or react with a transport species to form vapors, which condense into a liquid alloy. This process results in a precipitation of the crystals from the liquid alloy. The process shares a resemblance to VLS phase path. Yet, there are clear differences in the growth mechanism. For instance, VLS growth generally occurs at the liquid-solid interface and requires the metal to be saturated with the growing species. In the b-AsP crystal there is evidence that As deposits at around the same vertical position in the crystal. This could be due to the molten alloy reaching an As solubility limit upon cooling of the system that causes As precipitation. The finding that the As concentration in the solid does not depend on the amount of As in the ampule supports the idea that the As concentration in the melt has reached its solubility limit for the conditions used and is not kinetically limited. VLS for 2D crystals can occur laterally along the substrate surface however the classic metal bulb at the liquid-solid interface can be seen upon cooling down.36

The analysis techniques used here provide ample evidence to compare the b-P and b-AsP growth mechanisms. We observe three major differences between the two growth processes: the preferred growth axis, nucleation process, and the presence of a Sn-O-P sublayer with large voids. These differences arise in spite of the fact that the b-AsP CVT growth technique is the same as the b-P growth technique except for the addition of g-As. Both b-P and b-AsP crystal growth results in high aspect dimensions of ~10:1, however, the preferred (longest) growth axis is different for the two materials. The nucleation center for b-P was concluded to be the SnI<sub>x</sub> crystallites present vertically along the b-P crystal. The b-AsP crystals show no sign of SnI<sub>x</sub> in the crystal. Instead, there are As deposits in the lower region of the b-AsP crystal. The As particles do not appear to be a nucleation center site because they are contained to a small region of the overall crystal and do not appear to have any epitaxial interface. The void-containing layer beneath the b-AsP crystal, which we suggest may be a low-Tg binary SnO2-P2O5 glass, shows only a trace of arsenic when EDS is conducted. However, no void layer forms when b-P is grown on a similar wafer. It is not clear how the presence of As leads to the formation of a Sn-O-P mixture with large voids. Since the thermal oxide shows no sign of degradation, we postulate that the oxygen for this layer comes from the surface of the ampule. Finally, we suggest that the voids may represent bubbles of gasses such as P<sub>2</sub>O<sub>5</sub> trapped inside this molten glass as it solidifies.

## 4. Conclusion

Black arsenic phosphorus (b-AsP) single crystals are fabricated directly onto a silicon wafer using the b-P technique outline in previous work. Hero flakes are 12 x 110 microns single crystals that are 200 nm thick. CS-TEM has provided valuable insight into the crystal growth process. A Sn layer surrounds the entirety of the crystal and As deposits are found in a thin region of the cross-section. Raman spectroscopy determined the characteristic Raman modes for b-P and b-AsP that are consistent with reported literature. XPS verify that the composition of the grown b-AsP material is consistent with trends in the relative Raman peaks for the three zones of b-AsP Raman spectra. EBSD was essential in determining the crystallographic axis of the material, which, found that the preferred axis for b-Asp is along the arm-chair axis. CS-TEM showed the presence of Sn at the surface of the b-AsP growth. Arsenic particles are present in the b-AsP crystal lattice. We believe that this is due to stress-induced precipitation caused by the introduction of As into the b-P lattice. Lastly, a Sn-O-P layer with large voids is found between the b-AsP crystal and the grown SiO2 layer. Thin film transistor devices were fabricated from exfoliated bulk-b-AsP grown in the same conditions as the thin film growth process are characterized.

### **Author Contributions**

N.I. and S.A.C. conceived and designed the project and data analysis. J.C.M. carried out all CS-TEM sample preparation, CS-TEM experiments and CS-TEM data analysis. N.C.A.S. carried out the EBSD experiment and data analysis. P.G. fabricated the devices and performed electrical characterization, while P. G. and S.J.K. analyzed the electrical data. N.I. and S.A.C. wrote the manuscript with contributions from all authors.

# Notes

The authors declare no competing financial interest.

# **Acknowledgements**

Portions of this work were conducted in the Minnesota Nano Center, which is supported by the National Science Foundation (NSF) through the National Nano Coordinated Infrastructure Network, under Award ECCS-1542202. N.I.

also received support from this award. P.G. and S.J.K. acknowledge support by the NSF under Award ECCS-1708769. Parts of this work were supported by the Partnership for Research and Education in Materials (PREM) Program of the National Science Foundation under Award Number DMR-1523577. Parts of this work were carried out in the Characterization Facility, University of Minnesota, which receives partial support from NSF through the MRSEC program, under Award DMR-1420013.

# References

- (1) Katsnelson, M. I.; Fasolino, A. Graphene: Basic Properties; pp 7–24.
- Novoselov, K. S.; Mishchenko, A.; Carvalho, A.; Neto, A. H. C.; Castro Neto, A. H.; Neto, A. H. C.; Castro Neto, A. H. 2D Materials and van Der Waals Heterostructures.
  Science (80-.). 2016, 353, 1–25.
- (3) Liu, B.; Köpf, M.; Abbas, A. N.; Wang, X.; Guo, Q.; Jia, Y.; Xia, F.; Weihrich, R.; Bachhuber, F.; Pielnhofer, F.; Wang, H.; Dhall, R.; Cronin, S. B.; Ge, M.; Fang, X.; Nilges, T.; Zhou, C. Black Arsenic-Phosphorus: Layered Anisotropic Infrared Semiconductors with Highly Tunable Compositions and Properties. Adv. Mater. 2015, 27, 4423–4429.
- (4) Castellanos-Gomez, A. Black Phosphorus: Narrow Gap, Wide Applications. J. Phys. Chem. Lett. 2015, 6, 4280– 4291.
- (5) Kistanov, A. A.; Cai, Y.; Zhou, K.; Dmitriev, S. V.; Zhang, Y. W. The Role of H2O and O2 Molecules and Phosphorus Vacancies in the Structure Instability of Phosphorene. 2D Mater. 2017, 4.
- (6) Edmonds, M. T.; Tadich, A.; Carvalho, A.; Ziletti, A.; O'Donnell, K. M.; Koenig, S. P.; Coker, D. F.; Ozyilmaz, B.; Neto, A. H. C.; Fuhrer, M. S.; ??zyilmaz, B.; Neto, A. H. C.; Fuhrer, M. S. Creating a Stable Oxide at the Surface of Black Phosphorus. ACS Appl. Mater. Interfaces 2015, 7, 14557–14562.
- (7) Favron, A.; Gaufrès, E.; Fossard, F.; Phaneuf-L'Heureux, A.-L.; Tang, N. Y.-W.; Lévesque, P. L.; Loiseau, A.; Leonelli, R.; Francoeur, S.; Martel, R.; Phaneuf-L'Heureux, A.-L.; Tang, N. Y.-W.; Lévesque, P. L.; Loiseau, A.; Leonelli, R.; Francoeur, S.; Martel, R.; Phaneuf-L'Heureux, A.-L.; Tang, N. Y.-W.; et al. Photooxidation and Quantum Confinement Effects in Exfoliated Black Phosphorus. *Nat. Mater.* 2015, *14*, 826–832.
- (8) Huang, Y.; Qiao, J.; He, K.; Bliznakov, S.; Sutter, E.; Chen, X.; Luo, D.; Meng, F.; Su, D.; Decker, J.; Ji, W.; Ruoff, R. S.; Sutter, P. Degradation of Black Phosphorus (BP): The Role of Oxygen and Water. 2015.
- (9) Abellán, G.; Wild, S.; Lloret, V.; Scheuschner, N.; Gillen, R.; Mundloch, U.; Maultzsch, J.; Varela, M.; Hauke, F.; Hirsch, A. Fundamental Insights into the Degradation and Stabilization of Thin Layer Black Phosphorus. *J. Am. Chem. Soc.* 2017, 139, 10432–10440.
- (10) Luxa, J.; Bouša, D.; Zoller, F.; Fattakhova-Rohlfing, D.; Sofer, Z. Black Phosphorus- Arsenic Alloys for Lithium Ion Batteries. *FlatChem* 2019, 19, 100143.
- (11) Wu, R. J.; Topsakal, M.; Low, T.; Robbins, M. C.; Haratipour, N.; Jeong, J. S.; Wentzcovitch, R. M.; Koester,

- S. J.; Mkhoyan, K. A. Atomic and Electronic Structure of Exfoliated Black Phosphorus Atomic and Electronic Structure of Exfoliated Black Phosphorus. *J. Vac. Sci. Technol. A* **2015**, *33*, 060604.
- (12) Osters, O.; Nilges, T.; Bachhuber, F.; Pielnhofer, F.; Weihrich, R.; Schöneich, M.; Schmidt, P. Synthesis and Identification of Metastable Compounds: Black Arsenic-Science or Fiction? *Angew. Chemie Int. Ed.* 2012, 51, 2994–2997.
- (13) Zhong, M.; Xia, Q.; Pan, L.; Liu, Y.; Chen, Y.; Deng, H. X.; Li, J.; Wei, Z. Thickness-Dependent Carrier Transport Characteristics of a New 2D Elemental Semiconductor: Black Arsenic. Adv. Funct. Mater. 2018, 28, 1–8.
- (14) Yun, H.; Ghosh, S.; Golani, P.; Koester, S. J.; Mkhoyan, K. A. Layer Dependence of Dielectric Response and Water-Enhanced Ambient Degradation of Highly Anisotropic Black As. ACS Nano 2020.
- (15) Golani, P.; Yun, H.; Ghosh, S.; Wen, J.; Mkhoyan, A.; Koester, S. J. Ambipolar Transport in van Der Waals Black Arsenic Field Effect Transistors. *Nanotechnology* 2020.
- (16) Ichimin Shirotani, Junya Mikami, Takafumi Adachi, Yoshinori Katayama, Kazuhiko Tsuji, Haruki Kawamura, Osamu Shimomura, and T. N. Phase Transitions and Superconductivity of Black Phosphorus and Phosphorus-Arsenic Alloys at Low Temperatures and High Pressures. 1994, 50, 274–278.
- (17) Antonatos, N.; Luxa, J.; Sturala, J.; Sofer, Z. Black Arsenic: A New Synthetic Method by Catalytic Crystallization of Arsenic Glass. *Nanoscale* **2020**, 2–6.
- (18) phosphorus https://webbook.nist.gov/cgi/inchi/InChI%3D1S/P (accessed Mar 15, 2020).
- (19) Seidl, M.; Balázs, G.; Scheer, M. The Chemistry of Yellow Arsenic. Chem. Rev. 2019, 119, 8406–8434.
- Young, E. P.; Park, J.; Bai, T.; Choi, C.; DeBlock, R. H.; Lange, M.; Poust, S.; Tice, J.; Cheung, C.; Dunn, B. S.; Goorsky, M. S.; Ozolinš, V.; Streit, D. C.; Gambin, V. Wafer-Scale Black Arsenic-Phosphorus Thin-Film Synthesis Validated with Density Functional Perturbation Theory Predictions. ACS Appl. Nano Mater. 2018, 1, 4737–4745.
- (21) Izquierdo, N.; Myers, J. C.; Seaton, N. C. A.; Pandey, S. K.; Campbell, S. A. Thin-Film Deposition of Surface Passivated Black Phosphorus. ACS Nano 2019, 13, 7091–7099.
- (22) Wang, D.; Yi, P.; Wang, L.; Zhang, L.; Li, H.; Lu, M.; Xie, X.; Huang, L.; Huang, W. Revisiting the Growth of Black Phosphorus in Sn-I Assisted Reactions. *Front. Chem.* 2019, 7, 1–9.
- (23) RRUFF Database: Raman, X-Ray, Infrared and Chemistry https://rruff.info/arsenolamprite/display=default/.
- (24) Sugai, S. Raman and Infrared Reflection Spectroscopy in Black Phosphorus. *Solid State Commun.* **1985**, *53*, 753–755.
- (25) Chen, Y.; Chen, C.; Kealhofer, R.; Liu, H.; Yuan, Z.; Jiang, L.; Suh, J.; Park, J.; Ko, C.; Choe, H. S.; Avila, J.; Zhong, M.; Wei, Z.; Li, J.; Li, S.; Gao, H.; Liu, Y.; Analytis, J.; Xia, Q.; et al. Black Arsenic: A Layered Semiconductor with Extreme In-Plane Anisotropy. *Adv. Mater.* 2018, 30, 1–6.
- (26) Golani, P.; Yun, H.; Ghosh, S.; Wen, J.; Mkhoyan, A.; Koester, S. J. Ambipolar Transport in van Der Waals Black Arsenic Field Effect Transistors. *Nanotechnology* 2020, 31.

- (27) Lim, J. W. (Austin). The Properties and Structure of Tin Phosphate Glasses Modified with Other Oxides, Missouri University of Science and Technology, 2010.
- (28) Binnewies, M.; Glaum, R.; Schmidt, M.; Schmidt, P. *Chemical Vapor Transport Reactions*; 2012.
- (29) Wagner, R. S.; Ellis, W. C. Vapor-Liquid-Solid Mechanism of Single Crystal Growth. Appl. Phys. Lett. 1964, 4, 89–90.
- (30) Fujiwara, S.; Namikawa, Y.; Nakamura, T.; Tatsumi, M. Growth of Large ZnSe Single Crystal by R-CVT Method. J. Cryst. Growth 2005, 275, 415–419.
- (31) Fiechter, S.; Eckert, K. Crystal Growth of HfS2 by Chemical Vapour Transport with Halogen (Cl, Br, I). *J. Cryst. Growth* **1988**, *88*, 435–441.
- (32) Wang, D.; Luo, F.; Lu, M.; Xie, X.; Huang, L.; Huang, W. Chemical Vapor Transport Reactions for Synthesizing Layered Materials and Their 2D Counterparts. Small 2019, 15, 1–12.
- (33) Zhao, M.; Niu, X.; Guan, L.; Qian, H.; Wang, W.; Sha, J.; Wang, Y. Understanding the Growth of Black Phosphorus Crystals. CrystEngComm 2016, 18, 7737–7744.
- (34) Ek, M.; Filler, M. A. Atomic-Scale Choreography of Vapor-Liquid-Solid Nanowire Growth. Acc. Chem. Res. 2018, 51, 118–126.
- (35) Schmidt, V.; Wittemann, J. V.; Gösele, U. Growth, Thermodynamics, and Electrical Properties of Silicon Nanowires. Chem. Rev. 2010, 110, 361–388.
- (36) Li, S.; Lin, Y.-C.; Liu, X.; Hu, Z.; Liu, S.; Nakajima, H.; Okazaki, T.; Wu, J.; Chen, W.; Minari, T.; Sakuma, Y.; Tsukagoshi, K.; Suenaga, K.; Taniguchi, T.; Osada, M. Wafer-Scale and Deterministic Patterned Growth of Monolayer MoS2 via Vapor-Liquid-Solid Method. Nanoscale 2019, No. August.